

Self-Anti-Stacking 2D Metal Phosphide Loop-Sheet Heterostructures by Edge-Topological Regulation for Highly Efficient Water Oxidation

Quan Quan, Zhengxun Lai, Yan Bao, Xiuming Bu, You Meng, Wei Wang, Tsunaki Takahashi, Takuro Hosomi, Kazuki Nagashima, Takeshi Yanagida, Chuntai Liu, Jian Lu, and Johnny C. Ho*

2D metal phosphide loop-sheet heterostructures are controllably synthesized by edge-topological regulation, where Ni₂P nanosheets are edge-confined by the N-doped carbon loop, containing ultrafine NiFeP nanocrystals (denoted as NiFeP@NC/Ni₂P). This loop-sheet feature with lifted-edges prevents the stacking of nanosheets and induces accessible open channels for catalytic site exposure and gas bubble release. Importantly, these NiFeP@NC/Ni₂P hybrids exhibit a remarkable oxygen evolution activity with an overpotential of 223 mV at 20 mA cm⁻² and a Tafel slope of 46.1 mV dec⁻¹, constituting the record-high performance among reported metal phosphide electrocatalysts. The NiFeP@NC/Ni₂P hybrids are also employed as both anode and cathode to achieve an alkaline electrolyzer for overall water splitting, delivering a current density of 10 mA cm⁻² with a voltage of 1.57 V, comparable to that of the commercial Pt/C||RuO₂ couple (1.56 V). Moreover, a photovoltaic–electrolysis coupling system can as well be effectively established for robust overall water splitting. Evidently, this ingenious protocol would expand the toolbox for designing efficient 2D nanomaterials for practical applications.

system still lies in the sluggish oxygen evolution reaction (OER) because of its high energy barrier for the O–H bond breaking and the attendant O–O bond formation.^[2] In this regard, efficient OER electrocatalysts are urgently required to address this challenge by effectively utilizing multiple proton and electron transfers for oxygen evolution at low overpotentials.^[3,4] At present, many noble metal catalysts (e.g., RuO₂ and IrO₂) are well-acknowledged to be efficient for OER, but they can hardly satisfy the scale-up applications due to their scarcity and high cost.^[5] Recently, cost-effective and highly efficient non-noble-metal alternatives, transition metal phosphides (TMPs), have been emerged as a new family of OER catalysts.^[6] Although there are significant progresses achieved in exploiting these advanced phosphide nanostructures for efficient OER, their OER performance is quite far from satisfactory.

Electrocatalytic water splitting powered by renewable energy sources is considered as an attractive technology to produce clean fuels, which can relieve the ever-growing energy demands from fossil fuels and the associated environmental crisis.^[1] However, the bottleneck for a fully integrated water-splitting

In general, ingeniously engineering the TMPs with well-defined geometries and functional nanoarchitectures has been demonstrated as an effective method to promote their electrocatalytic activities.^[7,8] For the most part, 2D TMP nanosheets offer unique properties originating from their ultrathin

Q. Quan, Z. Lai, Dr. X. Bu, Y. Meng, W. Wang, Prof. J. C. Ho
Department of Materials Science and Engineering
City University of Hong Kong
Hong Kong SAR 999077, China
E-mail: johnnyho@cityu.edu.hk

Dr. Y. Bao, Prof. J. Lu
Department of Mechanical Engineering
City University of Hong Kong
Hong Kong SAR 999077, China

Dr. T. Takahashi, Dr. T. Hosomi, Dr. K. Nagashima,
Prof. T. Yanagida
Department of Applied Chemistry
School of Engineering
University of Tokyo
Tokyo 113-8654, Japan

 The ORCID identification number(s) for the author(s) of this article can be found under <https://doi.org/10.1002/smll.202006860>.

DOI: 10.1002/smll.202006860

Prof. T. Yanagida, Prof. J. C. Ho
Institute for Materials Chemistry and Engineering
Kyushu University
Fukuoka 816-8580, Japan

Prof. C. Liu
Key Laboratory of Advanced Materials Processing & Mold (Zhengzhou University)
Ministry of Education
Zhengzhou 450002, China

Prof. J. Lu
Centre for Advanced Structural Materials
City University of Hong Kong Shenzhen Research Institute
Greater Bay Joint Division
Shenyang National Laboratory for Materials Science
Shenzhen 518057, China

Prof. J. C. Ho
State Key Laboratory of Terahertz and Millimeter Waves
City University of Hong Kong
Hong Kong SAR 999077, China

thickness, large surface area, and high surface-to-volume atom ratios, which are beneficial for enhancing the active site exposure and enlarging the contact between reactant molecules and active sites to boost their OER performance.^[9–11] Despite the great promise, the 2D structural precursors tend to easily aggregate or sinter due to lattice strains arising from heteroatom substitution (i.e., phosphorus) and stochastic strain release during the phase transformation process.^[12] In this way, these 2D phosphide nanosheets or nanoplates are typically in situ grown on conductive substrates for immobilization, where the material growth is highly dependent on the external media, limiting their versatile utilization. On the other hand, the freestanding 2D nanosheets are usually inclined to stack together through the weak van der Waals interaction to form bundles and agglomerations, severely compromising the electrochemical properties.^[13,14] Considering the instability during synthetic processes and the intrinsic stacking problem, rationally appending building blocks anchored onto the periphery of 2D nanosheets by a targeted edge-topologic regulation is anticipated to be a multieffective strategy to resolve these issues; meanwhile, the synchronously aroused electronic structure modulation can further optimize the electrocatalytic performance of the nanosheets.^[15]

Here, for the first time, as a proof of concept, we have edge-selectively grown the Ni–Fe PBA nanocubes along the periphery of ultrathin Ni(OH)₂ nanosheets by controlling the coordination reaction kinetics in order to construct a loop-sheet heterostructure. During the phosphorization step, the edge-loop topology is found to compensate the stress induced in the phase transformation process. In this case, the obtained metal phosphides are well-maintained with their 2D heterostructure, in which the interconnected polycrystalline Ni₂P nanoparticles as sheet structures are edge-confined by the N-doped carbon loop containing ultrafine uniform NiFeP nanocrystals (denoted as NiFeP@NC/Ni₂P). Benefiting from the conspicuously accessible active sites and the largely improved mass/charge transfer based on the self-anti-stacking loop-sheet heterostructures, the achieved NiFeP@NC/Ni₂P exhibits an overpotential of 223 mV at a current density of 20 mA cm⁻² and a small Tafel slope of 46.1 mV dec⁻¹, ranking the top tier among the state-of-the-art metal phosphide electrocatalysts reported to date. Importantly, the NiFeP@NC/Ni₂P couple can also be employed as bifunctional catalysts to drive the overall water splitting in alkaline solution, requiring a cell voltage of 1.57 V and 1.83 V at 10 mA cm⁻² and 100 mA cm⁻², respectively. A solar-cell-driven overall water-splitting device is as well constructed to illustrate its effective and robust operation. As a result, the controllable synthetic methodology developed in this work would pave a new way to synthesize versatile and efficient 2D-morphological TMP heterostructure, which does not only enrich the 2D material family but also significantly promote their practical use for a wide range of energy and environment-related applications.

Figure 1a schematically illustrates the two-step preparation procedure of the NiFeP@NC/Ni₂P loop-sheet heterostructure. The Ni–Fe PBA/Ni(OH)₂ loop-sheet precursors are first constructed through the [Fe(CN)₆]³⁺ coordinating with the edge-released Ni²⁺ ions from ultrathin Ni(OH)₂ nanosheets under the assistance of H⁺, followed by the phosphorization treatment via a gas-solid reaction. At first, as shown in the

field-emission scanning electron microscopy (FESEM) image in Figure 1b, the starting Ni(OH)₂ precursor is confirmed to have a high 2D anisotropy with a lateral dimension of ≈400 nm. The atomic force microscopy (AFM) image reveals the thickness of Ni(OH)₂ being ≈2.5 nm, demonstrating its ultrathin nanosheet structure (Figure S1, Supporting Information).^[12] Next, under the assistance of exotic H⁺ and [Fe(CN)₆]³⁺ species at 40 °C, the Ni–Fe PBA nanocubes are in situ and directionally grown on the peripheral edge of Ni(OH)₂ nanosheets (Figure 1c and Figure S2, Supporting Information). The X-ray powder diffraction (XRD) results of the obtained samples further illustrate additional patterns of the face-centered cubic structure of Ni–Fe PBAs assigned to Ni₃[Fe(CN)₆]₂ phase (JCPDS No. 46-0906) besides the peaks of Ni(OH)₂ (JCPDS No. 14-0117), confirming the formation of pure Ni–Fe PBA phase onto Ni(OH)₂ nanosheets (Figure 1d).^[12,16] Moreover, as compared with the Raman peaks of Ni(OH)₂, the obtained spectrum of Ni–Fe PBA/Ni(OH)₂ shows an additional band at ≈2250 cm⁻¹, which is corresponded to the vibrational frequency of C–N bond (Figure S3, Supporting Information),^[17] being in good agreement with the XRD results.

The control experiments and temperature-dependent reactions are then carried out to unravel the underlying growth mechanism of Ni–Fe PBA. To be specific, without the addition of [Fe(CN)₆]³⁺ species, the size of Ni(OH)₂ nanosheets exhibits a shrinkage and their edges become rough and irregular as only reacting with H⁺ (Figure S4a,b, Supporting Information), manifesting the Ni²⁺ being etched from the edge of Ni(OH)₂ nanosheets. This observation is in conformity with the previous report that the edge is more vulnerable than smooth plane surface under H⁺ attack owing to more exposed defects in the edge.^[18] In addition, when [Fe(CN)₆]³⁺ is only participated in the reaction without adding H⁺, the sparse Ni–Fe PBA nanocubes are randomly dispersed on the Ni(OH)₂ nanosheets (Figure S4c,d, Supporting Information) and the corresponding XRD pattern of Ni–Fe PBA phase is not discerned because of the sluggish production rate (Figure S5, Supporting Information). It is disclosed that the H⁺ is essential for the edge-selectivity etch. For comparison, the exotic Ni²⁺ using NiCl₂ as a source is directly utilized to react with [Fe(CN)₆]³⁻ instead of applying Ni(OH)₂ nanosheets as the template. In this way, the pure Ni–Fe PBA is formed, which is confirmed by the XRD pattern (Figure S6a, Supporting Information). However, the pure Ni–Fe PBA is present in the form of severely aggregative particles (Figure S6b, Supporting Information), demonstrating that it is beneficial for the synthesis of well-ordered Ni–Fe PBA nanocubes through dissolving the Ni²⁺ from Ni(OH)₂ nanosheets by H⁺ etching.^[19] At the same time, the temperature-dependent reactions are further performed to explore the different reaction stages for the formation of Ni–Fe PBA/Ni(OH)₂. Explicitly, as compared with the as-prepared product at 40 °C, the smaller and discrete Ni–Fe PBA nanocubes are anchored on the edge of Ni(OH)₂ obtained at the lower temperature (i.e., 20 °C) (Figure S7a,b, Supporting Information), while the bigger and much more PBA nanocubes are formed and thus cover the Ni(OH)₂ surface at the higher temperature (i.e., 60 °C) (Figure S7c,d, Supporting Information). All these findings are also supported by the gradually increased XRD diffraction intensity of Ni₃[Fe(CN)₆]₂ in Figure S8 (Supporting Information) as

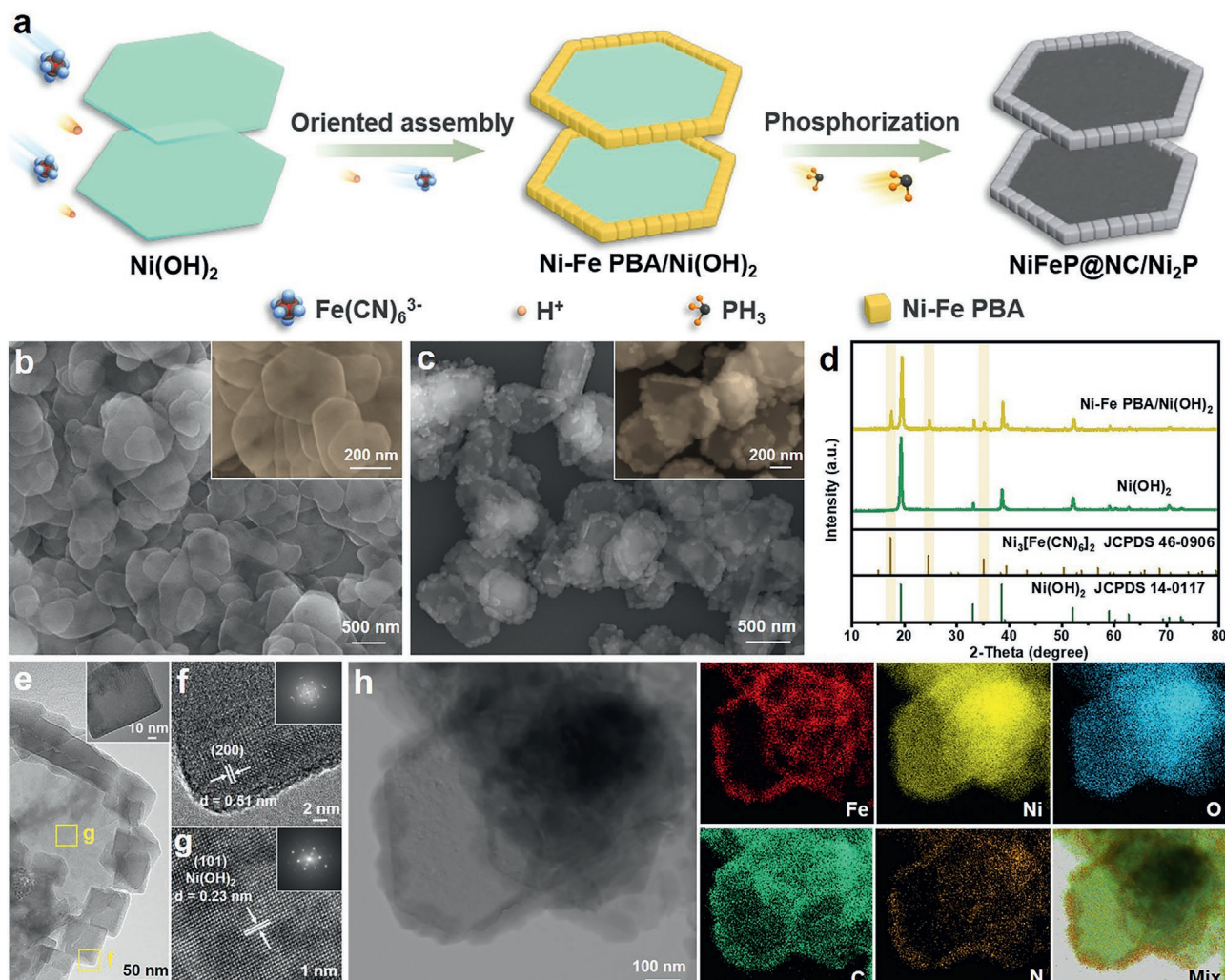


Figure 1. a) Schematic illustration of the preparation process of NiFeP@NC/Ni₂P loop-sheet heterostructures. FESEM images of b) Ni(OH)₂ nanosheets and c) Ni-Fe PBA/Ni(OH)₂. d) XRD patterns of Ni(OH)₂ and Ni-Fe PBA/Ni(OH)₂. e) TEM image of Ni-Fe PBA/Ni(OH)₂ (Inset: TEM image of a single Ni-Fe PBA nanocube). HRTEM images of f) the single Ni-Fe PBA nanocube and g) the Ni(OH)₂ in Ni-Fe PBA/Ni(OH)₂ heterostructure (Inset: FFT patterns of the Ni-Fe PBA nanocube and Ni(OH)₂, respectively). h) STEM-EDX element mapping of Ni-Fe PBA/Ni(OH)₂.

well as their color change from the light green of Ni(OH)₂ into yellow brown in Figure S9 (Supporting Information).

Above all, the above results evidently indicate that this coordination reaction initially occurred at the edge of nanosheets with the assistance of foreign H⁺.^[20] In detail, the Ni²⁺ ions released from edge sites would in situ coordinate with [Fe(CN)₆]³⁻ to form Ni-Fe PBA nanocubes at the solid-liquid interface (Figure S10, Supporting Information). Also, the reaction rate is highly dependent on the reaction temperature.^[21] The Ni-Fe PBA/Ni(OH)₂ synthesized at 40 °C displays that the well-ordered Ni-Fe PBA nanocubes are edge-selectively aligned on the Ni(OH)₂ nanosheets and the phosphatized product exhibits the optimal catalytic activity; therefore, the obtained product is chosen as the typical sample for the subsequent characterization. Notably, the AFM image of such Ni-Fe PBA/Ni(OH)₂ heterostructure illustrates the height of two overlapped loop-sheets gets increased to two orders of magnitudes more than that of the two overlapped ultrathin Ni(OH)₂ nanosheets (Figure S11, Supporting Information). This increase of the height is due

to the lifted-edges formed by the Ni-Fe PBA loop, where the loop prevents the 2D plane-to-plane stacking and induce the construction of open channels.

To get more insights into the detailed structure achieved by the edge-selective synthesis strategy, transmission electron microscopy (TEM) and energy-dispersive X-ray (EDX) elemental mapping are conducted. As depicted in Figure 1e, each individual PBA nanocube, also attaching with neighboring nanocubes, is implanted along the edge of sheet-template to construct a cube-to-loop architecture. Besides, high-resolution TEM (HRTEM) images in Figure 1f,g are recorded from the edge and surface region marked by the yellow frames in Figure 1e, respectively. In region f, the lattice spacing is determined to be 0.51 nm, which is attributed to the (200) face of Ni-Fe PBA (Figure S12, Supporting Information).^[22] The corresponding fast Fourier transform (FFT) pattern presents distinct bright spots with a cubically arranged shape (the inset of Figure 1f), suggesting the formation of pure Ni-Fe phase and being consistent with the XRD results.^[22] Simultaneously,

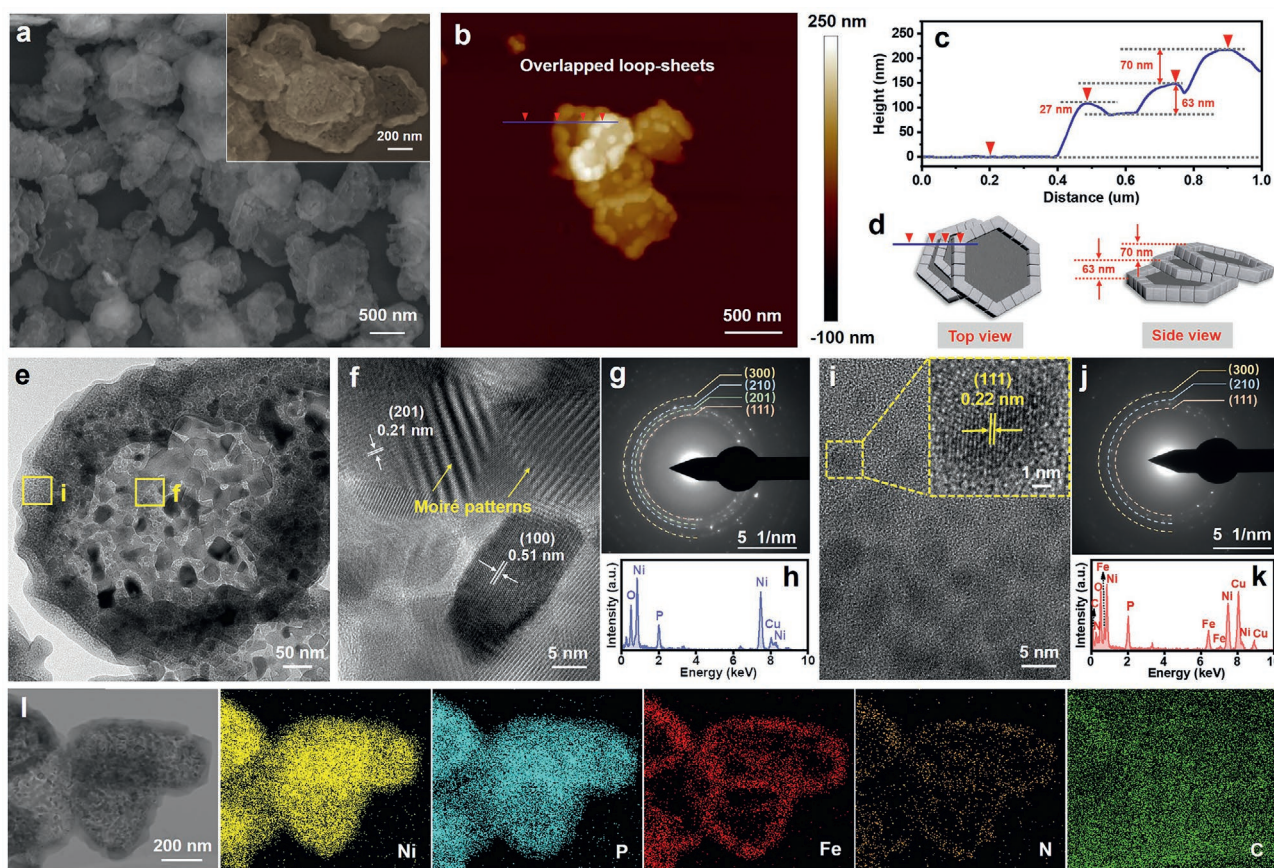


Figure 2. Structural characterization of NiFeP@NC/Ni₂P heterostructures. a) SEM image. b) AFM image of overlapped NiFeP@NC/Ni₂P loop-sheet heterostructures c) with corresponding height profile and d) schematic illustrations. e) TEM image. f) HRTEM image, g) SAED pattern, and h) EDX spectrum of the selected plane structure in NiFeP@NC/Ni₂P heterostructures. i) HRTEM image, j) SAED pattern, and k) EDX spectrum of the selected loop structure in NiFeP@NC/Ni₂P heterostructures. l) STEM-EDX elemental mapping of NiFeP@NC/Ni₂P loop-sheet heterostructures.

the well-resolved lattice fringes with a spacing of 0.23 nm can be indexed to the (101) planes of Ni(OH)₂ in the region g (Figure S13, Supporting Information).^[12] The single crystalline nature of Ni(OH)₂ nanosheets is evidently validated by its FFT pattern (the inset of Figure 1g). Moreover, the scanning TEM (STEM) and the corresponding EDX mapping are employed to evaluate the spatial element distribution in this heterostructure (Figure 1h).^[7] It is witnessed that the Fe, C, and N elements clearly occupy the edges. Also, the O element is evenly distributed across the subsheet while the Ni element is stretched through the entire loop-sheet structure, corroborating that the edge-etching Ni²⁺ ions from Ni(OH)₂ nanosheets are indeed coordinated with [Fe(CN)₆]³⁺. Therefore, the above results can jointly affirm the successful edge-selective formation of Ni-Fe PBA loop onto Ni(OH)₂ nanosheets.

After that, the obtained Ni-Fe PBA/Ni(OH)₂ loop-sheet hybrids are phosphatized via a facile gas-solid phase reaction to form NiFeP@NC/Ni₂P. The typical SEM images of final products suggest that the loop-sheet heterostructure is well inherited with the rough surface (Figure 2a and Figure S14, Supporting Information). The corresponding AFM image further reveals the lifted-edges at the periphery of nanosheets (Figure 2b,c), illustrating the geometrically restricted stacking property and the concurrently formed open channels for

effective gas release (Figure 2d). The XRD pattern of hexagonal Ni₂P (JCPDS No. 89-2742) is well discerned without diffraction peaks of precursors remained, manifesting the complete transformation of Ni-Fe PBA/Ni(OH)₂ after the phosphorization process (Figure S15, Supporting Information). Notably, the pure Ni₂P diffraction peaks do not only represent the phosphorization of Ni(OH)₂ but also indicate a single-phase matter of NiFeP originated from Ni-Fe PBA rather than from a mixture of two solid phases,^[23] which is resulted from the coexistence of Ni and Fe atoms in Ni-Fe PBA and their synchronous phase transformation.^[24] As a comparison, the XRD pattern of pure Ni-Fe PBA after phosphorization reveals the coexistence of two-phase separated Ni₂P (JCPDS No. 89-2742) and FeP (JCPDS No. 65-2595), which can be attributed to the different stoichiometric ratio of elements in the precursors (Figure S16, Supporting Information).^[25] The TEM analysis is as well conducted to trace the changes of phase and interior structure for the as-obtained NiFeP@NC/Ni₂P hybrid. As displayed in Figure 2e, an individual loop-sheet heterostructure discloses that the subsheet is consisted of an assembly of arbitrarily oriented and interconnected Ni₂P nanoparticles with a high density of interparticle grain boundaries, thereby fully activating the basal planes. Besides, the ultrafine NiFeP nanocrystals are confined in the amorphous N-doped carbon loop derived from the Ni-Fe

PBA cube-to-loop architecture, endowing abundant active sites distributed at edge-loop as well. The marked plane region f and loop region i in Figure 2e are further characterized, respectively. In Figure 2f, the HRTEM image of the plane region illustrates that the interplanar spacing of the nanoparticles are 0.21 and 0.51 nm, corresponding to the (201) and (100) planes of Ni₂P crystals, accordingly.^[26] It is interesting that Moiré patterns can be clearly distinguished because of the overlap of Ni₂P nanoparticles at small mis-orientation angles, which designate the lattice distortion of Ni₂P obtained from the phosphorization process of single crystal Ni(OH)₂.^[27,28] The corresponding selected-area electron diffraction (SAED) image suggests its polycrystalline structure (Figure 2g), while the EDX spectrum implies the existence of Ni, P, and O elements (Figure 2h). The O element is come from the surface oxidation of Ni₂P due to air exposure.^[29,30] Meanwhile, the HRTEM image of the loop region in Figure 2i delineates that the ultrafine nanocrystals are dotted among the amorphous N-doped carbon matrix with an average diameter of ≈3.2 nm (Figure S17, Supporting Information). Besides, the distinguished lattice fringes of 0.22 nm can be ascribed to the (111) plane of NiFeP crystals.^[31] The SAED patterns and EDX spectrum of this marked loop region signify the polycrystalline structure of NiFeP nanocrystals and the coexistence of Ni, Fe, P, N, and O elements, respectively (Figure 2j,k), demonstrating that the Fe element is still located at loop region after phosphorization. The STEM-EDX elemental mapping also demonstrates the homogeneous distribution of Ni and P elements and the distinctly edge-occupied Fe, N, C elements (Figure 2l). All these confirm the fully inherited loop-sheet heterostructure and spatial element distribution after phosphorization reaction. Additionally, the incorporation of carbon matrix is further verified by Raman spectroscopy. The two broad peaks centered at around 1350 cm⁻¹ (D band) and 1560 cm⁻¹ (G band) are observed to confirm the presence of carbonaceous species in this NiFeP@NC/Ni₂P heterostructure, which can be credited to the carbonization of cyano groups of Ni-Fe PBA (Figure S18, Supporting Information).^[4,32,33]

For a comparison, the pure Ni(OH)₂ nanosheets are as well directly undergone phosphorization reaction under identical conditions. As expected, the obtained Ni₂P product is failed to maintain the nanosheet shape and fall apart as severely aggregated nanoparticles owing to their random stress transfer in the interior to reach a mechanical equilibrium (Figure S19, Supporting Information).^[12] In this way, it is revealed that the edged-loop is crucial to facilitate the stress transfer and compensate the stress derived from the lattice mismatch in the phase transformation process. Therefore, the 2D nanosheet structure of as-obtained interconnected Ni₂P nanoparticles with abundant grain boundaries is well preserved, contributing to the exposure of solution-accessible active sites. Moreover, the two counterparts (i.e., Ni-Fe PBA/Ni(OH)₂-20 and Ni-Fe PBA/Ni(OH)₂-60, where the numbers of 20 and 60 designate the synthesis temperature) are gone through the identical phosphorization process. Their corresponding products (i.e., NiFeP@NC/Ni₂P-20 and NiFeP@NC/Ni₂P-60) present the well-maintained 2D heterostructure as disclosed by the overview SEM images (Figure S20, Supporting Information), further indicating the confined effect of the Ni-Fe PBA subarchitecture in order to maintain the 2D structure. In particular,

the HRTEM images and STEM-EDX elemental mapping of NiFeP@NC/Ni₂P-20 demonstrate the well-defined loop-sheet heterostructure and the distinctly edge-occupied Fe element, further validating the efficient stress-relaxation effect of the edged Ni-Fe PBA architecture during the phase transformation process from Ni(OH)₂ to Ni₂P (Figure S21, Supporting Information).

Collectively, the above characterization results illustrate three aspects of the structural information: i) The Ni-Fe PBA nanocubes are edge-selectively implanted along the periphery of ultrathin Ni(OH)₂ nanosheets, topologically lifting the edges to prevent sheet-to-sheet stacking; ii) after phosphorization, the interconnected Ni₂P nanoparticles with abundant grain boundaries maintain the 2D sheet structure and simultaneously activate the basal planes, while the Ni-Fe PBA cube-to-loop architecture is converted into N-doped carbon loop decorated with ultrafine NiFeP nanocrystals rendering abundant active sites distributed at edge-loop as well; iii) the obtained NiFeP@NC/Ni₂P is well-maintained with its 2D loop-sheet heterostructure owing to the edged-loop topology compensating the stress induced in the phase transformation process.

To shed light on the valence states and electronic structure of NiFeP@NC/Ni₂P, the detailed X-ray photoelectron spectroscopy (XPS) analysis is performed. The survey XPS spectra are collected to convey the coexistence of Ni, Fe, P, C, and N in NiFeP@NC/Ni₂P as well as O elements due to the inevitable surface oxidation of phosphides coming from air exposure (Figure S22a, Supporting Information).^[34] The depth-profiling XPS spectra of Ni 2p can be deconvoluted into four peaks besides the satellites (Figure 3a). During Ar ion sputtering, it is observed that the intensity of the two peaks at 852.9 (Ni 2p_{3/2}) and 870.2 eV (Ni 2p_{1/2}) for Ni²⁺ in Ni-P gets gradually increased, which confirms the interior existing in the form of phosphides.^[12] Simultaneously, the intensity of other two peaks at 856.8 (Ni 2p_{3/2}) and 874.6 eV (Ni 2p_{1/2}) decreases because the oxidized Ni species (Ni³⁺) located at surface would contact with the ambient air rather than the interior.^[35] For the case of Fe, similar changes in the depth-profiling XPS spectra of Fe 2p suggest the intrinsic phosphide to form NiFeP with surface oxidation as well (Figure S22b, Supporting Information).^[36,37] The intensity of P-M (M = Ni, Fe) bond is increased for the increasing Ar ion sputtering duration, agreeing well with the above discussion (Figure S22c, Supporting Information).^[38] It is also noted that the depth-profiling N 1s and C 1s spectra signify the uniform distribution of N-doped carbon matrix (Figure S22d,e, Supporting Information), being consistent with the Raman and EDX element mapping results discussed above. As compared with the interior valence states and chemical environment of Ni₂P, the binding energies of Ni 2p and P 2p for NiFeP@NC/Ni₂P are shifted negatively, indicating the charge redistribution occurs after introducing the edge NiFeP@NC loop due to the strong interfacial interaction (Figure 3b,c).^[39] Such effects suggest the strong electronic coupling of Ni₂P nanosheet and NiFeP@NC loop, which is beneficial for electron transport during OER.^[40]

With the aim to further assess the subtle change in the electronic state for the loop-sheet heterostructure, element-selective X-ray absorption fine structure (XAFS) spectroscopy experiments are conducted, including X-ray absorption near-edge structure (XANES) and extended X-ray absorption fine

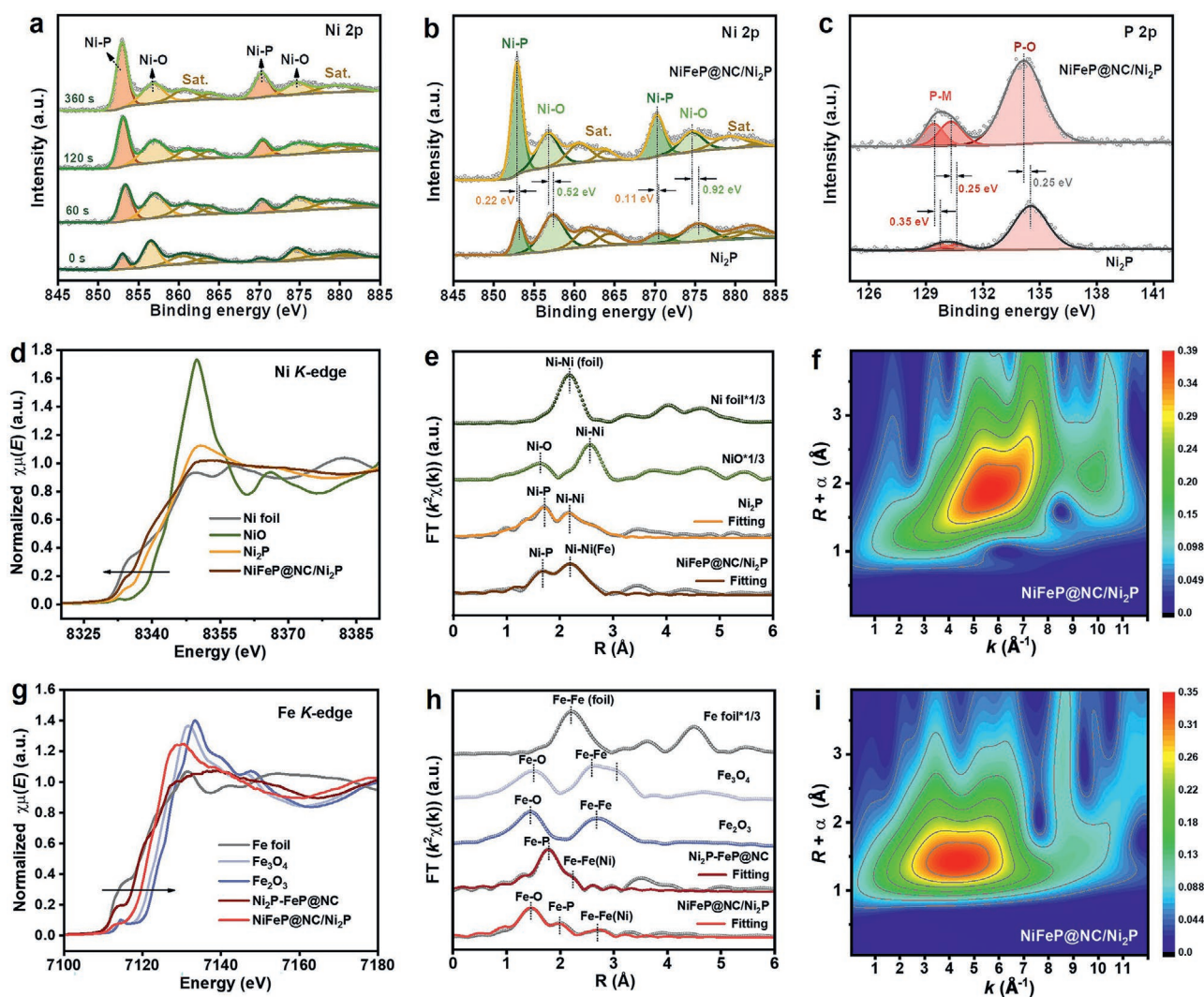


Figure 3. a) Depth-profiling XPS spectra of Ni 2p for NiFeP@NC/Ni₂P after Ar ion etching with different duration. High-resolution XPS for b) Ni 2p and c) P 2p spectra of NiFeP@NC/Ni₂P and Ni₂P under Ar ion etching for 360 s. d) Ni K-edge XANES spectra. e) Fourier transform of Ni K-edge EXAFS spectra at R space and the corresponding EXAFS fitting at R space. f) Wavelet transform of the k²-weighted EXAFS data of NiFeP@NC/Ni₂P. g) Fe K-edge XANES spectra. h) Fourier transform of Fe K-edge EXAFS spectra at R space and the corresponding EXAFS fitting at R space. i) Wavelet transform of the k²-weighted EXAFS data of NiFeP@NC/Ni₂P.

structure (EXAFS).^[41,42] Figure 3d shows the Ni K-edge XANES spectra of NiFeP@NC/Ni₂P, Ni₂P, NiO, and Ni foil. The absorption edges of NiFeP@NC/Ni₂P and Ni₂P are found lower than that of NiO but higher than the one of Ni foil, which indicates the average charge state values of Ni element in NiFeP@NC/Ni₂P and Ni₂P being less than +2.^[43] Moreover, as compared with Ni₂P, a negative edge shift of XANES peak of NiFeP@NC/Ni₂P is observed along with a decrease of the Ni oxidation state, indicating the occurrence of electron transfer to Ni sites and engendering the electron enrichment on the Ni sites.^[44,45] The reverse trend is observed for the positive edge shift of the Fe K-edge XANES spectra of NiFeP@NC/Ni₂P as compared with that of Ni₂P-FeP@NC (Figure 3g). It confirms the oxidation state of Fe increased in the edge NiFeP@NC loop, which is beneficial for the oxidation reaction.^[46] Also, a comparison of the Fourier transforms of EXAFS and fitting results at the Ni K-edge of the different samples is applied to extract the

structural parameters (Figure 3e).^[47–48] The Ni–Ni(Fe) bond distance in NiFeP@NC/Ni₂P is slightly shorter than that of Ni₂P (Table S1, Supporting Information), meaning the Ni–Ni(Fe) bond strengthening and demonstrating an intimate interfacial contact of edge-occupied Fe species with interconnected Ni₂P nanoparticles.^[43,44] The Fourier transforms of EXAFS and fitting results at the Fe K-edge reveal a distinguished position difference of Fe–P and Fe–Fe(Ni) bond in NiFeP@NC/Ni₂P as compared with those in Ni₂P-FeP@NC (Figure 3h and Table S2, Supporting Information). This distinct difference indicates the dissimilar coordination spheres of Fe atoms, which in turn confirms the single-phase NiFeP existing in NiFeP@NC/Ni₂P as distinguished from the two-phase Ni₂P and FeP in Ni₂P-FeP@NC. The wavelet transform (WT) of Ni K-edge EXAFS oscillations of NiFeP@NC/Ni₂P demonstrates only one intensity maximum at 5.7 Å⁻¹ related to the Ni–P bonding, which is shifted to the larger value as compared

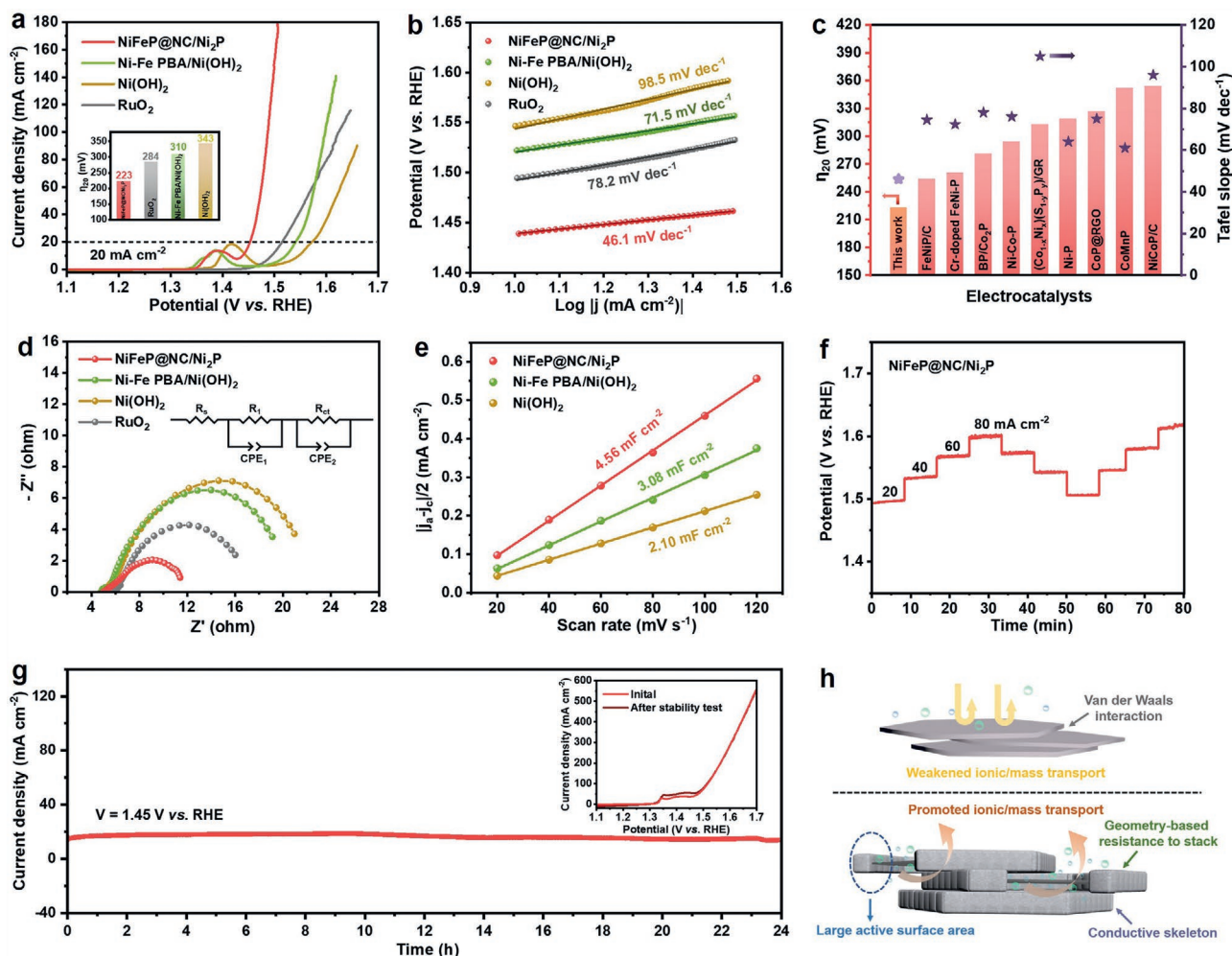


Figure 4. a) Polarization curves of NiFeP@NC/Ni₂P, Ni-Fe PBA/Ni(OH)₂, Ni(OH)₂, and RuO₂. b) The corresponding Tafel plots derived from the polarization curves in (a). c) Comparison of overpotentials at 20 mA cm⁻² and Tafel plots for NiFeP@NC/Ni₂P and other reported TMPs for OER. d) Nyquist plots of NiFeP@NC/Ni₂P, Ni-Fe PBA/Ni(OH)₂, Ni(OH)₂, and RuO₂ (Inset: equivalent circuit). e) The double-layer capacitance (C_{dl}) of NiFeP@NC/Ni₂P, Ni-Fe PBA/Ni(OH)₂, and Ni(OH)₂. f) Multicurrent steps chronopotentiometry curve of NiFeP@NC/Ni₂P without iR correction. g) Stability test of NiFeP@NC/Ni₂P on NF via chronoamperometry curve for 24 h without iR correction (Inset: polarization curves of NiFeP@NC/Ni₂P on NF before and after chronoamperometry measurement without iR correction). h) Schematic illustration of the comparison of 2D sheets and loop-sheets.

with that of Ni₂P (Figure 3f and Figure S23, Supporting Information).^[49] The WT of Fe K-edge EXAFS oscillations of NiFeP@NC/Ni₂P as well displays one intensity maximum at 4.2 Å⁻¹ assigned to the Fe-P coordination, which is shifted to a smaller value as compared with that of Ni₂P-FeP@NC (Figure 3i and Figure S24, Supporting Information).^[50] All these results clearly illustrate that the controllable construction of the edge-loop concurrently regulates the local electronic configuration in NiFeP@NC/Ni₂P heterostructure, which is conducive to oxidation reaction and electron transfer.

In this way, the electrocatalytic performance of NiFeP@NC/Ni₂P for OER is thoroughly evaluated by a typical three-electrode setup under alkaline condition (1 M KOH, pH 13.6). For a comparison, the obtained Ni-Fe PBA/Ni(OH)₂, Ni(OH)₂, and the commercial RuO₂ are measured at identical condition. As shown in Figure 4a, the polarization curve reveals that the as-obtained NiFeP@NC/Ni₂P exhibits an overpotential of 223 mV for OER at 20 mA cm⁻², which is much smaller

than those of Ni-Fe PBA/Ni(OH)₂ ($\eta_{20} = 310$ mV), Ni(OH)₂ ($\eta_{20} = 343$ mV) as well as the commercial RuO₂ ($\eta_{20} = 284$ mV). Moreover, the NiFeP@NC/Ni₂P product requires a much lower overpotential of 257 mV to afford a high current density of 100 mA cm⁻², whereas the commercial RuO₂ needs an overpotential of 394 mV to yield the same current density of 100 mA cm⁻². Besides, NiFeP@NC/Ni₂P shows a much enhanced mass activity at an overpotential of 300 mV, which is about 9, 21, and 45 times higher than those of the benchmark RuO₂, binary Ni-Fe PBA/Ni(OH)₂, and pristine Ni(OH)₂, respectively (Figure S25, Supporting Information). All these results suggest the ultrahigh efficiency of NiFeP@NC/Ni₂P for electrocatalytic OER. To further investigate the OER kinetics, the corresponding Tafel plots are measured. As displayed in Figure 4b, the Tafel slope of NiFeP@NC/Ni₂P is determined to be 46.1 mV dec⁻¹ that is much lower than those of RuO₂ (78.2 mV dec⁻¹), Ni-Fe PBA/Ni(OH)₂ (71.5 mV dec⁻¹), and Ni(OH)₂ (98.5 mV dec⁻¹), implying the favorable OER kinetics of

the NiFeP@NC/Ni₂P hybrids. The electrocatalytic OER activity of different counterparts are also measured under the identical alkaline condition. As a result, the NiFeP@NC/Ni₂P has superior OER performance than Ni₂P–FeP@NC ($\eta_{20} = 244$ mV; Tafel slope: 54.9 mV dec⁻¹), NiFeP@NC/Ni₂P-60 (249 mV; 64.5 mV dec⁻¹), NiFeP@NC/Ni₂P-20 (277 mV; 65.0 mV dec⁻¹), and Ni₂P (308 mV; 78.5 mV dec⁻¹) (Figures S26 and S27, Supporting Information). Those results corroborate that the synergistic composition effects of hybrid provide a crucial factor to the superior electrocatalytic OER performance,^[51] in which the edge-topologic regulation on NiFeP@NC/Ni₂P catalyst induces Ni₂P nanosheets confined by NiFeP@NC loop exhibiting the optimal synergistic effects of the components. Impressively, the low overpotential and Tafel slope point toward the OER performance of NiFeP@NC/Ni₂P being superior to almost all TMP catalysts reported previously, placing the NiFeP@NC/Ni₂P catalyst among the top tier of water oxidation catalysts (Figure 4c and Tables S3 and S4, Supporting Information).

On the other hand, to elucidate the origins of the high OER performance of NiFeP@NC/Ni₂P, we carry out the electrochemical impedance spectroscopy (EIS) and double-layer capacitance (C_{dl}) measurement. In explicit, EIS analysis is first employed to uncover the interfacial reaction kinetics. The Nyquist plot reveals that the NiFeP@NC/Ni₂P catalyst exhibits the lowest charge transfer resistance (4.5 Ω) as compared with those of RuO₂ (8.8 Ω), Ni–Fe PBA/Ni(OH)₂ (15.1 Ω), and Ni(OH)₂ (16.2 Ω), implying the superior charge-transfer capacity of NiFeP@NC/Ni₂P because the self-anti-stacking loop-sheet feature with lifted-edges can induce open channels to facilitate mass transfer (Figure 4d and Table S5, Supporting Information).^[52] Subsequently, the values of C_{dl} are measured to estimate the electrochemically active surface area (ECSA) in order to assess the corresponding intrinsic activity of OER electrocatalysts. The cyclic voltammetry (CV) curves of NiFeP@NC/Ni₂P, Ni–Fe PBA/Ni(OH)₂, and Ni(OH)₂ with different scan rates are recorded (Figure S28, Supporting Information). As presented in Figure 4e, the C_{dl} value of NiFeP@NC/Ni₂P is found to be 4.56 mF cm⁻², being larger than that of Ni–Fe PBA/Ni(OH)₂ (3.08 mF cm⁻²) and Ni(OH)₂ (2.10 mF cm⁻²). It is suggested that a higher density of catalytically active sites is obtained in NiFeP@NC/Ni₂P, which can be ascribed to the formation of abundant grain boundaries in the 2D Ni₂P sheet and the gain of ultrafine NiFeP nanocrystals in the edge-loop. More importantly, the loop-sheet structure can prevent the stacking of 2D nanosheets from blocking the active sites. Instead, it can create accessible open channels for the better exposure of these catalytic sites. In addition, Figure 4f illustrates the multistep chronopotentiometric curve of NiFeP@NC/Ni₂P with the current density increased stepwise from 20 to 80 mA cm⁻². Each increasing step, with a duration of 500 s, shows the instantly stable state as the current changes, verifying the excellent ion/mass transport (i.e., inward diffusion of OH⁻ and outward diffusion of oxygen bubbles) of NiFeP@NC/Ni₂P loop-sheet heterostructures with open channel construction.^[53,54]

The stability of NiFeP@NC/Ni₂P is further evaluated via a chronoamperometry curve for 24 h. It is noted that the Ni foam (NF) is used as the substrate for this stability test to prevent the catalyst from detachment during a long-time opera-

tion because the deposited catalyst would easily fall off from the small-area glass carbon electrode (GCE) under the influence of generated O₂ gas bubbles.^[55] As a result, the current remains constant without any obvious degradation in this long-duration electrochemical process, indicating an excellent stability of this NiFeP@NC/Ni₂P loop-sheet heterostructure (Figure 4g). The morphology of NiFeP@NC/Ni₂P subjected to the stability test is also examined. The corresponding TEM image illustrates the catalysts sustained the original framework, demonstrating the structural stability of such 2D loop-sheet heterostructures (Figure S29, Supporting Information). This enhanced stability is anticipated due to the fact that the N-doped carbon looped-skeleton would hold the sheet more robustly with strong mechanical reinforcement.^[56] Later, the processed NiFeP@NC/Ni₂P catalyst after OER stability test for 24 h is further characterized by the depth-profiling XPS to evaluate the OER mechanism (Figure S30a, Supporting Information).^[57] Specifically, without any Ar ion etching, the characteristic peaks related to Ni–P and Fe–P bonding are completely disappeared, whereas there are only the oxidized peaks observed in the Ni 2p and Fe 2p spectra (Figure S30b,c, Supporting Information), indicating the surface is completely oxidized on the phosphides after the reaction. It can be ascribed to the formation of oxy/hydroxides (M–OOH, M = Ni, Fe) as active sites for OER,^[58] which is consistent with the previous reports of TMPs for OER.^[59–61] Likewise, for P 2p spectrum without any Ar ion etching, the disappearance of the phosphide components (≈ 129 eV) further confirms the oxidation of phosphides on the surface (Figure S30d, Supporting Information).^[4] Furthermore, the peaks ascribed to Ni–P and Fe–P bonding in the Ni 2p and Fe 2p spectra, respectively, are present and intensified under the prolonged etching time, indicating the core materials remained unchanged.^[62] In this way, the OER catalytic capability of NiFeP@NC/Ni₂P for OER can be originated from the formation of catalytically active oxo/hydroxide on the surface. Previous computational study of (Ni,Fe)OOH has indicated that the converted Fe(IV) stabilizes the O radical by exchange interaction to generate it efficiently, while the Ni(IV) catalyzes the O–O coupling.^[63] The two components assume the two different critical functionalities necessitated for OER and this synergy can deliver the optimal OER performance.^[63,64] Alternatively, the core phosphides cooperated with the conductive carbonaceous looped-skeleton are particularly beneficial for the faster electron transport in the heterostructure.^[26,65]

Taken all together, the 2D loop-sheet heterostructure can effectively prevent sheet-to-sheet stacking with the lifted-edges, while the conventional 2D nanosheets are prone to stack together under the influence of van der Waals interaction,^[66,67] as schematically illustrated in Figure 4h. Therefore, this loop-sheet heterostructure is advantageous to the exposure of active sites and the enhanced contact area with electrolytes. Such structure with open channels can also promote the diffusion of water molecules and release of gaseous products to further avail the OER activity of catalysts. Apart from the exterior geometric superiority, the interior compositional synergism accompanied with electronic regulation is also critical to the excellent OER performance.^[68] Specifically, the N-doped carbon looped-skeleton can provide improved electrical conductivity, whereas the ultrafine NiFeP nanocrystals and Ni₂P nanoparticles

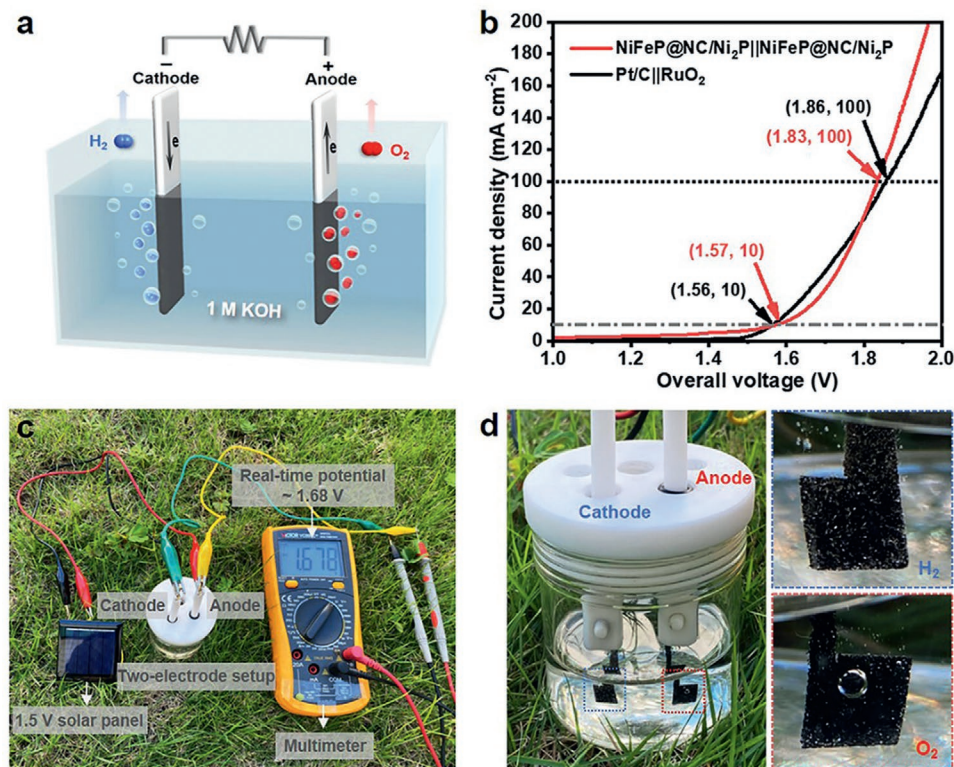


Figure 5. a) Schematic illustration of the two-electrode setup for overall water splitting. b) Polarization curves of NiFeP@NC/Ni₂P||NiFeP@NC/Ni₂P and Pt/C||RuO₂ in a two-electrode configuration for water splitting. c) Digital photograph of the NiFeP@NC/Ni₂P||NiFeP@NC/Ni₂P couple driven by a solar cell. d) Magnified photograph of the two-electrode setup and the electrodes.

provide abundant active Fe and Ni sites. Therefore, the appropriate control of NiFeP@NC edged-loop on the Ni₂P sheet can substantially lower the activation barrier with the optimal synergistic effect of Fe and Ni sites to achieve the superior OER performance of NiFeP@NC/Ni₂P.^[7,69]

The electrocatalytic hydrogen evolution reaction (HER) performance of NiFeP@NC/Ni₂P is also investigated in the alkaline solution (1 M KOH). It is found that the NiFeP@NC/Ni₂P catalyst exhibits an overpotential of 257 mV to afford a current density of 10 mA cm⁻² with outstanding stability for HER (Figure S31, Supporting Information). In this case, a two-electrode configuration employing NiFeP@NC/Ni₂P as both anode and cathode is constructed for overall water splitting in 1.0 M KOH electrolyte (Figure 5a). As shown in Figure 5b, the NiFeP@NC/Ni₂P couple shows a cell voltage of 1.57 V to reach a benchmark current density of 10 mA cm⁻², which is comparable to that of the commercial Pt/C||RuO₂ couple (1.56 V). It is noted that this voltage is lower than the simple addition of overpotentials from the HER and OER half-reaction, which could be ascribed to the fact that 3D NF as supporting electrode has a larger surface area and better electrical conductivity as compared with the ones of GCE.^[70] Notably, the NiFeP@NC/Ni₂P couple delivers a high current density of 100 mA cm⁻² achieved by a cell voltage of 1.83 V that is lower than that of Pt/C||RuO₂ (1.86 V). Furthermore, the durability of this electrolyzer is examined at a current density of 10 mA cm⁻². The chronopotentiometric curve illustrates that the NiFeP@NC/Ni₂P||NiFeP@NC/Ni₂P couple maintains a steady cell voltage at 10 mA cm⁻² over

24 h (Figure S32, Supporting Information), indicating the good mechanical robustness of NiFeP@NC/Ni₂P as bifunctional electrocatalysts. More importantly, this two-electrode device is also integrated with a commercial silicon solar cell to demonstrate the practical utilization of NiFeP@NC/Ni₂P for solar-driven water electrolysis. Interestingly, the NiFeP@NC/Ni₂P||NiFeP@NC/Ni₂P couple is efficiently powered by the solar panel, which provides a real-time potential output of ≈1.68 V under sunlight irradiation (Figure 5c). A large amount of bubbles is witnessed to be emerged from both electrodes (Figure 5d and Movie S1, Supporting Information). As a result, a solar-cell-driven overall water-splitting device can be effectively and robustly achieved by the NiFeP@NC/Ni₂P couple, which renders it with a good potential for industrial applications.

In summary, Ni-Fe PBA nanocubes are edge-selectively aligned along the periphery of ultrathin Ni(OH)₂ nanosheets to constitute a self-anti-stacking 2D loop-sheet assembly. The subsequent phosphorization treatment generates unique phosphides based heterostructures, with the architecture composing interconnected Ni₂P nanosheets and N-doped carbon loop decorated with ultrafine NiFeP nanocrystals. The key to this synthesis is owing to the edged-loop topology compensating the induced stress in the phase transformation process; therefore, the sheet-to-sheet stacking is prevented with lots of the open channels resulted. This edge-topologic and electronic regulation on the 2D metal phosphide heterostructure would contribute to the conspicuously accessible active sites and the largely improved ion/mass transfer. In this way, the

heterostructure exhibits a remarkable oxygen evolution activity with an overpotential of 223 mV at 20 mA cm⁻² and a small Tafel slope of 46.1 mV dec⁻¹, ranking the top tier among the metal phosphide electrocatalysts reported to date. Moreover, the NiFeP@NC/Ni₂P heterostructures are employed as both anode and cathode for overall water splitting in alkaline electrolytes, exhibiting a current density of 10 mA cm⁻² with a cell voltage of 1.57 V as well as excellent durability. More intriguingly, a solar-cell-driven overall water-splitting device can be robustly established based on the heterostructures. This work paves a promising pathway for preparing durable and vastly active 2D transition-metal heterostructures towards versatile applications in electrochemical energy storage and conversion.

Supporting Information

Supporting Information is available from the Wiley Online Library or from the author.

Acknowledgements

This work was financially supported by the National Natural Science Foundation of China (Grants 51672229), the General Research Fund (CityU 11204618) and the Theme-based Research (T42-103/16-N) of the Research Grants Council of Hong Kong SAR, China, the Science Technology and Innovation Committee of Shenzhen Municipality (Grant JCYJ20170818095520778), the Foshan Innovative and Entrepreneurial Research Team Program (No. 2018IT100031) as well as the City University of Hong Kong (Project No. 9610427).

Conflict of Interest

The authors declare no conflict of interest.

Keywords

bifunctional electrocatalysts, edge-selective synthesis, loop-sheets, overall water splitting, oxygen evolution reaction, transition metal phosphides

Received: November 3, 2020

Revised: December 8, 2020

Published online: January 22, 2021

- [1] B. You, Y. Sun, *Acc. Chem. Res.* **2018**, *51*, 1571.
- [2] K. Jiang, M. Luo, M. Peng, Y. Yu, Y.-R. Lu, T.-S. Chan, P. Liu, F. M. F. de Groot, Y. Tan, *Nat. Commun.* **2020**, *11*, 2701.
- [3] L.-A. Stern, L. Feng, F. Song, X. Hu, *Energy Environ. Sci.* **2015**, *8*, 2347.
- [4] X.-Y. Yu, Y. Feng, B. Guan, X. W. Lou, U. Paik, *Energy Environ. Sci.* **2016**, *9*, 1246.
- [5] D. Li, H. Baydoun, C. N. Verani, S. L. Brock, *J. Am. Chem. Soc.* **2016**, *138*, 4006.
- [6] M. Sun, H. Liu, J. Qu, J. Li, *Adv. Energy Mater.* **2016**, *6*, 1600087.
- [7] B. Qiu, L. Cai, Y. Wang, Z. Lin, Y. Zuo, M. Wang, Y. Chai, *Adv. Funct. Mater.* **2018**, *28*, 1706008.
- [8] H. Guo, Q. Feng, K. Xu, J. Xu, J. Zhu, C. Zhang, T. Liu, *Adv. Funct. Mater.* **2019**, *29*, 1903660.
- [9] D. Deng, K. S. Novoselov, Q. Fu, N. Zheng, Z. Tian, X. Bao, *Nat. Nanotechnol.* **2016**, *11*, 218.
- [10] W. Xu, F. Lyu, Y. Bai, A. Gao, J. Feng, Z. Cai, Y. Yin, *Nano Energy* **2018**, *43*, 110.
- [11] M. Zhao, Y. Huang, Y. Peng, Z. Huang, Q. Ma, H. Zhang, *Chem. Soc. Rev.* **2018**, *47*, 6267.
- [12] S.-H. Li, N. Zhang, X. Xie, R. Luque, Y.-J. Xu, *Angew. Chem., Int. Ed.* **2018**, *57*, 13082.
- [13] C. Tan, X. Cao, X.-J. Wu, Q. He, J. Yang, X. Zhang, J. Chen, W. Zhao, S. Han, G.-H. Nam, M. Sindoro, H. Zhang, *Chem. Rev.* **2017**, *117*, 6225.
- [14] J. Yu, Q. Wang, D. O'Hare, L. Sun, *Chem. Soc. Rev.* **2017**, *46*, 5950.
- [15] C. Hu, L. Zhang, Z. J. Zhao, A. Li, X. Chang, J. Gong, *Adv. Mater.* **2018**, *30*, 1705538.
- [16] X. Su, Y. Wang, J. Zhou, S. Gu, J. Li, S. Zhang, *J. Am. Chem. Soc.* **2018**, *140*, 11286.
- [17] K. W. Chapman, P. J. Chupas, C. J. Kepert, *J. Am. Chem. Soc.* **2006**, *128*, 7009.
- [18] X. Y. Yu, L. Yu, H. B. Wu, X. W. Lou, *Angew. Chem., Int. Ed.* **2015**, *54*, 5331.
- [19] Y. Zeng, G.-F. Chen, Z. Jiang, L.-X. Ding, S. Wang, H. Wang, *J. Mater. Chem. A* **2018**, *6*, 15942.
- [20] Y. Wang, J. Ma, J. Wang, S. Chen, H. Wang, J. Zhang, *Adv. Energy Mater.* **2019**, *9*, 1802939.
- [21] J. Nai, B. Y. Guan, L. Yu, X. W. D. Lou, *Sci. Adv.* **2017**, *3*, e1700732.
- [22] Z. Chen, B. Fei, M. Hou, X. Yan, M. Chen, H. Qing, R. Wu, *Nano Energy* **2020**, *68*, 104371.
- [23] R.-Q. Li, B.-L. Wang, T. Gao, R. Zhang, C. Xu, X. Jiang, J. Zeng, Y. Bando, P. Hu, Y. Li, X.-B. Wang, *Nano Energy* **2019**, *58*, 870.
- [24] G. Yilmaz, C. F. Tan, Y.-F. Lim, G. W. Ho, *Adv. Energy Mater.* **2019**, *9*, 1802983.
- [25] B. Cao, Y. Cheng, M. Hu, P. Jing, Z. Ma, B. Liu, R. Gao, J. Zhang, *Adv. Funct. Mater.* **2019**, *29*, 1906316.
- [26] F. Yu, H. Zhou, Y. Huang, J. Sun, F. Qin, J. Bao, W. A. Goddard, S. Chen, Z. Ren, *Nat. Commun.* **2018**, *9*, 2551.
- [27] X. Wang, Z. Wang, J. Zhang, X. Wang, Z. Zhang, J. Wang, Z. Zhu, Z. Li, Y. Liu, X. Hu, J. Qiu, G. Hu, B. Chen, N. Wang, Q. He, J. Chen, J. Yan, W. Zhang, T. Hasan, S. Li, H. Li, H. Zhang, Q. Wang, X. Huang, W. Huang, *Nat. Commun.* **2018**, *9*, 3611.
- [28] S. H. Lee, D. Y. Kim, J. Lee, S. B. Lee, H. Han, Y. Y. Kim, S. C. Mun, S. H. Im, T.-H. Kim, O. O. Park, *Nano Lett.* **2019**, *19*, 5437.
- [29] L. Yu, J. Zhang, Y. Dang, J. He, Z. Tobin, P. Kerns, Y. Dou, Y. Jiang, Y. He, S. L. Suib, *ACS Catal.* **2019**, *9*, 6919.
- [30] Q. Liang, L. Zhong, C. Du, Y. Luo, J. Zhao, Y. Zheng, J. Xu, J. Ma, C. Liu, S. Li, Q. Yan, *ACS Nano* **2019**, *13*, 7975.
- [31] W. Zhang, Y. Zou, H. Liu, S. Chen, X. Wang, H. Zhang, X. She, D. Yang, *Nano Energy* **2019**, *56*, 813.
- [32] Q. Quan, T. Zhang, C. Lei, B. Yang, Z. Li, J. Chen, C. Yuan, L. Lei, Y. Hou, *Nanoscale* **2019**, *11*, 22261.
- [33] P. Ge, S. Li, H. Shuai, W. Xu, Y. Tian, L. Yang, G. Zou, H. Hou, X. Ji, *Adv. Mater.* **2019**, *31*, 1806092.
- [34] F.-X. Ma, C.-Y. Xu, F. Lyu, B. Song, S.-C. Sun, Y. Y. Li, J. Lu, L. Zhen, *Adv. Sci.* **2019**, *6*, 1801490.
- [35] X. Wang, L. Chai, J. Ding, L. Zhong, Y. Du, T.-T. Li, Y. Hu, J. Qian, S. Huang, *Nano Energy* **2019**, *62*, 745.
- [36] Y. Wu, X. Tao, Y. Qing, H. Xu, F. Yang, S. Luo, C. Tian, M. Liu, X. Lu, *Adv. Mater.* **2019**, *31*, 1900178.
- [37] X. F. Lu, L. Yu, X. W. Lou, *Sci. Adv.* **2019**, *5*, eaav6009.
- [38] F. Yang, H. Gao, J. Hao, S. Zhang, P. Li, Y. Liu, J. Chen, Z. Guo, *Adv. Funct. Mater.* **2019**, *29*, 1808291.
- [39] S.-H. Yu, R. Wu, B. Xiao, Q. Gao, Y. Zheng, X. Zheng, J. Zhu, M.-R. Gao, *Angew. Chem., Int. Ed.* **2018**, *57*, 15445.
- [40] J.-X. Feng, S.-Y. Tong, Y.-X. Tong, G.-R. Li, *J. Am. Chem. Soc.* **2018**, *140*, 5118.
- [41] Y. Tong, Y. Guo, P. Chen, H. Liu, M. Zhang, L. Zhang, W. Yan, W. Chu, C. Wu, Y. Xie, *Chem* **2017**, *3*, 812.

- [42] L. Zhao, Y. Zhang, L.-B. Huang, X.-Z. Liu, Q.-H. Zhang, C. He, Z.-Y. Wu, L.-J. Zhang, J. Wu, W. Yang, L. Gu, J.-S. Hu, L.-J. Wan, *Nat. Commun.* **2019**, *10*, 1278.
- [43] E. Cao, Z. Chen, H. Wu, P. Yu, Y. Wang, F. Xiao, S. Chen, S. Du, Y. Xie, Y. Wu, Z. Ren, *Angew. Chem., Int. Ed.* **2020**, *59*, 4154.
- [44] Q. He, D. Tian, H. Jiang, D. Cao, S. Wei, D. Liu, P. Song, Y. Lin, L. Song, *Adv. Mater.* **2020**, *32*, 1906972.
- [45] D. Zhao, K. Sun, W. C. Cheong, L. Zheng, C. Zhang, S. Liu, X. Cao, K. Wu, Y. Pan, Z. Zhuang, B. Hu, D. Wang, Q. Peng, C. Chen, Y. Li, *Angew. Chem., Int. Ed.* **2020**, *59*, 8982.
- [46] X. Wang, Y. Jia, X. Mao, D. Liu, W. He, J. Li, J. Liu, X. Yan, J. Chen, L. Song, A. Du, X. Yao, *Adv. Mater.* **2020**, *32*, 2000966.
- [47] Y. Pan, K. Sun, Y. Lin, X. Cao, Y. Cheng, S. Liu, L. Zeng, W.-C. Cheong, D. Zhao, K. Wu, Z. Liu, Y. Liu, D. Wang, Q. Peng, C. Chen, Y. Li, *Nano Energy* **2019**, *56*, 411.
- [48] X. Liu, F. Liu, J. Yu, G. Xiong, L. Zhao, Y. Sang, S. Zuo, J. Zhang, H. Liu, W. Zhou, *Adv. Sci.* **2020**, *7*, 2001526.
- [49] J. Cai, Y. Song, Y. Zang, S. Niu, Y. Wu, Y. Xie, X. Zheng, Y. Liu, Y. Lin, X. Liu, G. Wang, Y. Qian, *Sci. Adv.* **2020**, *6*, eaaw8113.
- [50] H. Zhang, W. Zhou, J. Dong, X. F. Lu, X. W. Lou, *Energy Environ. Sci.* **2019**, *12*, 3348.
- [51] T. Liu, P. Li, N. Yao, G. Cheng, W. Luo, S. Chen, Y. Yin, *Angew. Chem., Int. Ed.* **2019**, *58*, 4679.
- [52] Y. Guo, J. Tang, Z. Wang, Y. Sugahara, Y. Yamauchi, *Small* **2018**, *14*, 1802442.
- [53] S. Gao, Y. Zhang, Y. Zhang, B. Wang, S. Yang, *Small* **2018**, *14*, 1804388.
- [54] X. Lu, C. Zhao, *Nat. Commun.* **2015**, *6*, 6616.
- [55] W. Ni, A. Krammer, C.-S. Hsu, H. M. Chen, A. Schüler, X. Hu, *Angew. Chem., Int. Ed.* **2019**, *58*, 7445.
- [56] J. Wang, D. Liu, H. Huang, N. Yang, B. Yu, M. Wen, X. Wang, P. K. Chu, X. F. Yu, *Angew. Chem., Int. Ed.* **2018**, *57*, 2600.
- [57] H. Q. Fu, L. Zhang, C. W. Wang, L. R. Zheng, P. F. Liu, H. G. Yang, *ACS Energy Lett.* **2018**, *3*, 2021.
- [58] H. J. Song, H. Yoon, B. Ju, G.-H. Lee, D.-W. Kim, *Adv. Energy Mater.* **2018**, *8*, 1802319.
- [59] L. Jiayuan, Y. Ming, Z. Xuemei, H. Zheng-Qing, X. Zhaoming, C. Chun-Ran, M. Yuanyuan, Q. Yongquan, *Adv. Funct. Mater.* **2016**, *26*, 6785.
- [60] H. B. Zhang, W. Zhou, J. Dong, X. F. Lu, X. W. D. Lou, *Energy Environ. Sci.* **2019**, *12*, 3348.
- [61] P. Ji, H. Jin, H. Xia, X. Luo, J. Zhu, Z. Pu, S. Mu, *ACS Appl. Mater. Interfaces* **2020**, *12*, 727.
- [62] J. Xu, X.-K. Wei, J. D. Costa, J. L. Lado, B. Owens-Baird, L. P. L. Gonçalves, S. P. S. Fernandes, M. Heggen, D. Y. Petrovykh, R. E. Dunin-Borkowski, K. Kovnir, Y. V. Kolen'ko, *ACS Catal.* **2017**, *7*, 5450.
- [63] H. Xiao, H. Shin, W. A. Goddard, *Proc. Natl. Acad. Sci USA* **2018**, *115*, 5872.
- [64] Y. Zhang, N. Li, Z. Zhang, S. Li, M. Cui, L. Ma, H. Zhou, D. Su, S. Zhang, *J. Am. Chem. Soc.* **2020**, *142*, 8490.
- [65] H. Liang, A. N. Gandi, D. H. Anjum, X. Wang, U. Schwingenschlög, H. N. Alshareef, *Nano Lett.* **2016**, *16*, 7718.
- [66] M. Qin, S. Li, Y. Zhao, C.-Y. Lao, Z. Zhang, L. Liu, F. Fang, H. Wu, B. Jia, Z. Liu, W. Wang, Y. Liu, X. Qu, *Adv. Energy Mater.* **2019**, *9*, 1803060.
- [67] J. Yang, Z. Zeng, J. Kang, S. Betzler, C. Czarnik, X. Zhang, C. Ophus, C. Yu, K. Bustillo, M. Pan, J. Qiu, L.-W. Wang, H. Zheng, *Nat. Mater.* **2019**, *18*, 970.
- [68] G. Guan, M.-Y. Han, *Adv. Sci.* **2019**, *6*, 1901837.
- [69] D. Friebe, M. W. Louie, M. Bajdich, K. E. Sanwald, Y. Cai, A. M. Wise, M. J. Cheng, D. Sokaras, T. C. Weng, R. Alonso-Mori, R. C. Davis, J. R. Bargar, J. K. Norskov, A. Nilsson, A. T. Bell, *J. Am. Chem. Soc.* **2015**, *137*, 1305.
- [70] Y. Lian, H. Sun, X. Wang, P. Qi, Q. Mu, Y. Chen, J. Ye, X. Zhao, Z. Deng, Y. Peng, *Chem. Sci.* **2019**, *10*, 464.